



## MATERIALS SCIENCE

# Dynamic interfacial electrostatic energy harvesting via a single wire

Lixia He<sup>1,2†</sup>, Yikui Gao<sup>1,2†</sup>, Di Liu<sup>1,2\*</sup>, Yuexiao Hu<sup>3</sup>, Jianxun Shi<sup>3</sup>, Jiayue Zhang<sup>4</sup>, Xinyuan Li<sup>1,2</sup>, Bingzhe Jin<sup>1,2</sup>, Baofeng Zhang<sup>5</sup>, Zhong Lin Wang<sup>1,6,7,8\*</sup>, Jie Wang<sup>1,2,6\*</sup>

Spontaneously occurred electrostatic breakdown releases enormous energy, but harnessing the energy remains a notable challenge due to its irregularity and instantaneity. Here, we propose a revolutionary method that effectively harvests the energy of dynamic interfacial electrostatic breakdown by simply imbedding a conductive wire (diameter, 25 micrometers) beneath dielectric materials to regulate the originally chaotic and distributed electrostatic energy resulted from contact electrification into aggregation, effectively transforming mechanical energy into electricity. A point-charge physical model is proposed to explain the power generation process and output characteristics, guide structural design, and enhance output performance. Furthermore, a quantified triboelectric series including 72 dielectric material pairs is established for materials choice and optimization. In addition, a high voltage of over 10 kilovolts is achieved using polytetrafluoroethylene and polyethylene terephthalate. This work opens a door for effectively using electrostatic energy, offering promising applications ranging from novel high-voltage power sources, smart clothing, and internet of things.

## INTRODUCTION

Static electricity is not only a ubiquitous phenomenon in our daily lives but also a well-documented scientific topic since ancient times, dating back to Thales of Miletus (1). The physical mechanism underlying the phenomenon is generally attributed to contact electrification (also known as triboelectrification) (2, 3), which typically occurs between two dielectric materials coming into contact and then separating, leading to the surfaces being positively and negatively charged. Despite the substantial power of electrostatic energy, its applications have been limited to only a few technologies (4, 5). This is primarily due to the large electric potential near charged surfaces (6, 7), which can cause electrostatic breakdown, resulting in a huge energy release with visible or invisible lights (8, 9), such as lightning and even x-ray with energies exceeding 10 keV (10). Despite numerous attempts reported over the past centuries to harness electrostatic energy (11), such as the famous experiment that extracted electricity from thunderclouds (12), successfully collecting the energy of lightning remains a challenge, especially given the irregularity, instantaneity, nonuniformity, and nondirectivity of electrostatic breakdown.

Recent achievements in triboelectric nanogenerator (TENG) (13–18) arising from triboelectrification and electrostatic breakdown have posed a prototype for harvesting the electrostatic energy of “artificial microlightning”—an elaborately designed discharge at microgaps between a charged dielectric material and a metal (19–21). Several

approaches to realizing performance improvement have been proposed including environmental control (22), configuration optimization (23–25), and materials selection (26, 27), as well as some derivative structural design such as microstructure combination (28), the introduction of side electrodes (29), etc. However, the interfacial electrostatic breakdown (IEB), which occurs spontaneously between triboelectric materials across the entire sliding interface rather than just in the predesigned breakdown domains (22, 30), significantly limits their output capability due to the wider breakdown scale and the resulting potentially stronger breakdown strength. Despite the significant amounts of energy contained of IEB, effective collection remains challenging because of its inherent characteristics of irregularity, instantaneity, nonuniformity, and nondirectivity. Furthermore, our recent work has revealed that the increased charge loss caused by IEB is further accelerated under large external loads (31), leading to a significant reduction in energy density. Consequently, how to regulate the IEB and to use its energy are always critically difficult problems, and there is still no good method to harvest this energy simply and effectively.

Here, we present a simple but efficient strategy for harnessing electrostatic energy generated by the IEB between two dielectric materials, which is realized only by deploying a conductive wire (diameter, 25  $\mu\text{m}$ ) beneath the dielectric materials. The buried conductive wire successfully regulates the distributed IEB and timely obtains electrostatic energy arising from IEB based on electrostatic induction. Moreover, we introduce a point-charge physical model to explain the above process and reveal its physical mechanism of collecting electrostatic energy from IEB. A quantified triboelectric series between two dielectric materials, including 72 material pairs, is also established for guiding the practical materials choice, and a high voltage over 10 kV is obtained by polytetrafluoroethylene (PTFE) and polyethylene terephthalate (PET). Consequently, the high voltage generated by electrostatic energy can successfully light 3024 light-emitting diodes (LEDs) and treat air pollution effectively, with the device area of 24  $\text{cm}^2$ , and the electric energy converted by electrostatic energy can efficiently power electronics with an optimized power management circuit (PMC) (energy conversion efficiency, 87.3%) based on a new signal processing

<sup>1</sup>Beijing Institute of Nanoenergy and Nanosystems, Chinese Academy of Sciences, Beijing 101400, P. R. China. <sup>2</sup>College of Nanoscience and Technology, University of Chinese Academy of Sciences, Beijing 100049, P. R. China. <sup>3</sup>Center on Nanoenergy Research, School of Physical Science and Technology, Guangxi University, Nanning, 530004, P. R. China. <sup>4</sup>Department of Mechanical Engineering, Tsinghua University, Beijing 100084, P. R. China. <sup>5</sup>Hubei Key Laboratory of Automotive Power Train and Electronic Control, School of Automotive Engineering, Hubei University of Automotive Technology, Shiyan 442002, P. R. China. <sup>6</sup>Guangzhou Institute of Blue Energy, Knowledge City, Huangpu District, Guangzhou 510555, P. R. China. <sup>7</sup>Georgia Institute of Technology, Atlanta, GA 30332, USA. <sup>8</sup>Yonsei Frontier Lab, Yonsei University, Seoul 03722, Republic of Korea.

\*Corresponding author. Email: liudi@binn.cas.cn (D.L.); zhong.wang@mse.gatech.edu (Z.L.W.); wangjie@binn.cas.cn (J.W.)

†These authors contributed equally to this work.

mode. The simple design of single conductive wire makes it an excellent candidate for seamless integration into wearable fabrics, collecting human mechanical energy for powering electronics with good air permeability and moisture resistance. This work provides a new direction for efficient energy conversion using electrostatic energy from dynamic IEB, which is promising in the field of novel high-voltage power sources, smart clothing, and internet of things.

## RESULTS

### IEB and the design of IEB-TENG

Electrostatic breakdown is a ubiquitous phenomenon in our daily life, including the lightning in nature, electrostatic discharge in factories, spark discharge in human everyday activities, and even the gap of two charged materials (Fig. 1A), which is usually considered as a negative effect, and the released energy may bring immeasurable losses. Specifically, according to the air breakdown theory, Paschen's law (Fig. 1B) (8, 9), the electric field between two charged materials can reach the threshold of electrostatic breakdown even if the separation distance ( $<60 \mu\text{m}$ ) and charge density ( $<250 \mu\text{C m}^{-2}$ ) are in a very small situation, which is the main reason for the frequent and easy occurrence of electrostatic breakdown. Undeniably, because of the different flatnesses of films, microgaps at the interface, and the high surface charge density on dielectric materials, IEB inevitably occurs in dissimilar materials (figs. S1 and S2 and note S1). Figure 1C and movie S1 show the irregular and powerful IEB phenomenon between various materials in our daily life (note S3), no matter what materials they are, such as fabric raw materials, industrial raw materials, and other organic films. This strong and universal IEB is unpredictable, nonuniform, and nondirectional and certainly causes huge energy loss.

Although IEB seems irregular and difficult to harvest its electrostatic energy, we find that it can approach and gather to a conductive wire (Fig. 1D, <i>). No matter where the conductive wire is located, the convergence phenomenon always happens during the dynamic process of IEB (movie S2). These results show that the IEB can be well regulated by a single conductive wire (Fig. 1D, <ii>), making the originally chaotic and distributed IEB into aggregation (fig. S3 and note S2). Moreover, the introduction of conductive wire alters the local curvature of dielectric surface covering it and may form ridges (fig. S4), which is a favorable factor in triggering discharge (fig. S5 and note S3). On the basis of this characteristic, a simple but efficient structure to successfully regulate IEB and harvest its electrostatic energy arising from dynamic IEB is proposed (Fig. 1E and fig. S4), which consists of three parts: a stator (the material of stator is PTFE), a slider [the material of slider is polyamide (PA)], and a single conductive wire. The conductive wire can not only regulate the distribute IEB into aggregation but also timely produce electricity arising from dynamic IEB, synergistically based on the triboelectrification, electrostatic breakdown, and electrostatic induction.

Given that the structure for harvesting the energy of dynamic IEB is related to contact electrification in nanoscale (32, 33), it is still named as a new type of TENG: IEB-TENG. In general, electrostatic breakdown and electrostatic induction simultaneously exist in the process of triboelectrification of TENGs (Fig. 1G). For conventional TENGs, the collected energy relies primarily on electrostatic induction, and IEB often has a negative impact on its performance (Fig. 1H, <i>, fig. S7, and note S5). For IEB-TENGs, the collected energy relies primarily on electrostatic breakdown; thus, IEB could

have a positive impact on its performance (Fig. 1H, <ii>), which removes the limitations imposed by IEB on the performance of conventional TENGs. Therefore, it achieves an average power density up to  $2.02 \text{ W m}^{-2} \text{ Hz}^{-1}$ , which is 18.7 times that of single-electrode TENG (S-TENG) and 5.4 times that of freestanding TENG (FS-TENG) (Fig. 1F, figs. S8 to S10, and note S6).

### The working principle and basic output characteristics of IEB-TENG

The IEB-TENG for harvesting electrostatic energy arising from dynamic IEB with boosted performance works via a new working mechanism. On the basis of triboelectrification, the surface of PA and PTFE are charged positively and negatively, respectively (Fig. 2A, <i>). Because of the different flatnesses of films, there are inevitably tiny gaps at the interface. When the PA slider moves forward, the strong electric field will be built in these gaps due to the separation of positive and negative charges, resulting in powerful IEB (fig. S11). Meanwhile, the conductive wire buried beneath the PTFE timely harvests energy arising from the strong IEB by electrostatic induction. Through triboelectrification and electrostatic breakdown, the net positive and negative charge domains are respectively formed at the front and back of the slider (note S7) (30). Given that the conductive wire is connected to the ground and at the zero potential, the direction of output current depends on the position of the conductive wire in potential regions (Fig. 2A, <ii>). It is clear that the conductive wire gradually passes from the positive potential region to the negative potential region when the slider moves from left to right, so an ac is produced. A simplified point-charge physical model is helpful for understanding its working principle (Fig. 2B and note S7).

The process of electron flow in IEB-TENG per cycle is shown in Fig. 2C. When the slider moves right (Fig. 2C, <i> and <ii>), electrons flow from the ground to the conductive wire because the wire is in the positive potential region, producing the positive output current (Fig. 2D, <ii>). Then, when the slider continues to move right (Fig. 2C, <iii>), the conductive wire is in the near-zero potential region, so there is no current flow at this region (Fig. 2D, <iii>). If the conductive wire enters to the negative potential region (Fig. 2C, <iv>), then the flowing direction of electrons is reversed, from the conductive wire to the ground, producing the negative output current (Fig. 2D, <iv>). Moreover, when the slider moves left, the conductive wire still passes through the three different potential regions in turn (Fig. 2C, <vi> to <viii>), producing the similar output current (Fig. 2D, <vi> to <viii>) (detailed working mechanism can be found in fig. S12 and note S8). Furthermore, the output signal characteristics of IEB-TENG with multiple wires further confirm the point-charge physical model (figs. S13 and S14 and note S9).

Specifically, the potential distribution at the front and back of slider is opposite, and once the moving direction of the slider changes, the direction of output current is also reversed. To further demonstrate these points, a surface potential measurement equipment is constructed (Fig. 2E) (30, 34, 35). There are two electrodes (electrode ① and electrode ②) mounted on the front and back ends of the slider (Fig. 2E, <i>), which are respectively connected to electrostatic voltmeters for surface potential measurement. Here, triboelectric materials of the slider and stator are PA and PTFE, respectively. When the slider moves right, through triboelectrification and electrostatic breakdown, electrode ① shows positive potential, and electrode ② shows negative potential (Fig. 2E, <ii>);

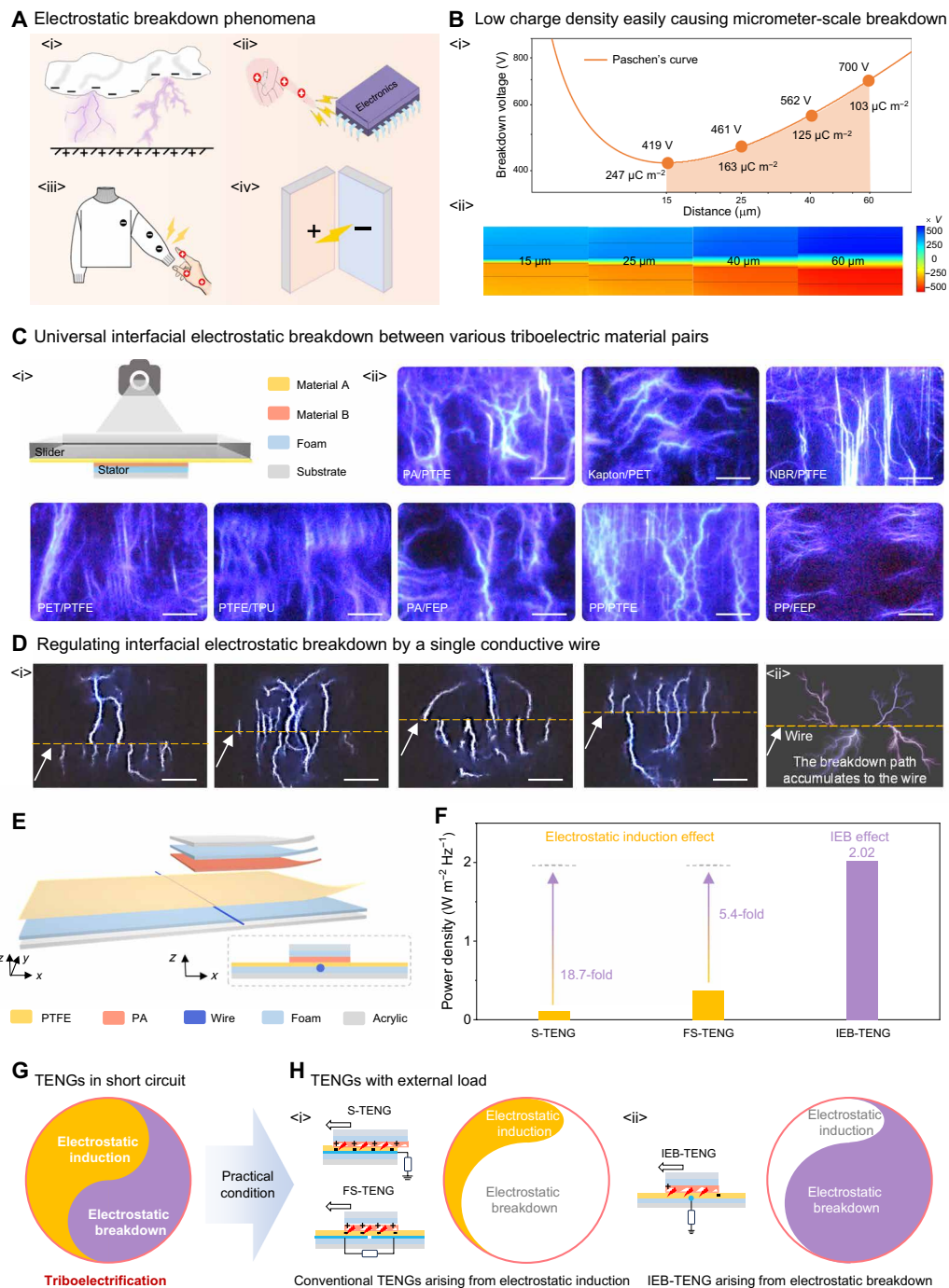


**Fig. 1. Electrostatic breakdown phenomena and IEB.** (A) Various electrostatic breakdown phenomena in nature. <i> Lightning in nature; <ii> electrostatic discharge in factories; <iii> spark discharge in dry winter; <iv> discharge between two charged materials. (B) Air breakdown theory to describe the electrostatic breakdown phenomenon around the micrometer scale. <i> The Paschen's curve; <ii> simulated results show the charge density of critical surface for electrostatic breakdown at different distances. It is clear that even minute quantities of charges can cause electrostatic breakdown in several micrometers to dozens of micrometer range. (C) Universal IEB between various triboelectric material pairs. <i> Hardware settings of the discharge observation experiments; <ii> photos of the IEB between different materials (scale bars, 1 cm). NBR, nitrile butadiene rubber; TPU, thermoplastic urethane; FEP, fluorinated ethylene propylene; PP, polypropylene. (D) IEB can be regulated by a single conductive wire (diameter, 25  $\mu\text{m}$ ). <i> Photos show that the scattered IEB gradually becomes concentrated because of the existed conductive wire (scale bars, 1 cm); <ii> the schematic diagram shows that the breakdown path accumulates to the conductive wire. (E) The schematic diagram of IEB-TENG, which can harvest the released energy of IEB. (F) Comparison of the output average power density between IEB-TENG and conventional TENGs. (G) Schematic diagram shows the relationship between electrostatic induction and electrostatic breakdown under short-circuit condition. (H) Comparison of conventional TENGs and IEB-TENG with load. <i> The enhanced electrostatic breakdown in load situation limits the output performance of conventional TENGs (arising from electrostatic induction); <ii> the enhanced electrostatic breakdown in load situation promotes the output performance of IEB-TENG (arising from electrostatic breakdown).

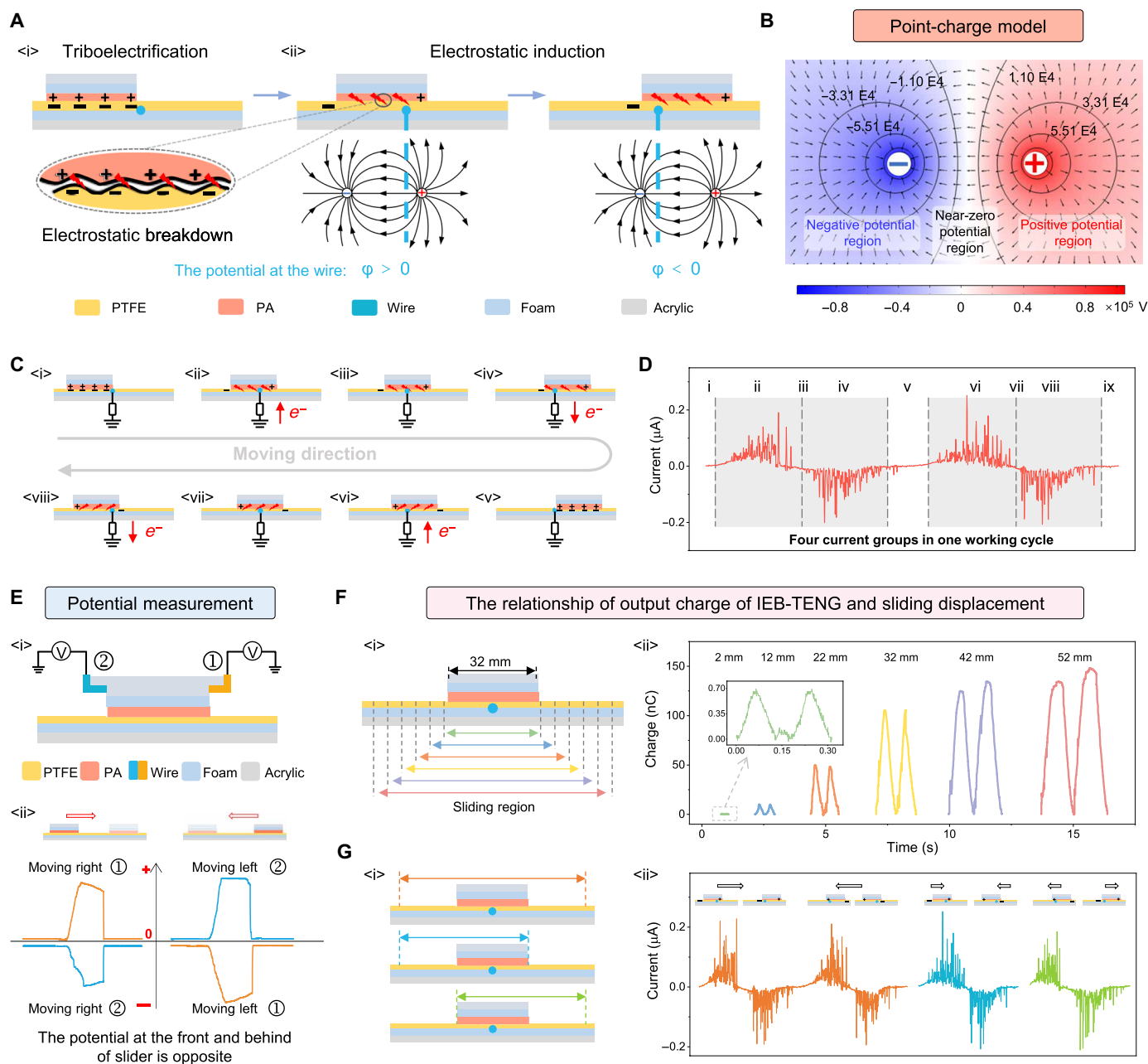


**Fig. 2. The working principle and basic output characteristics of IEB-TENG.** (A) Working mechanism of the IEB-TENG. (B) Simulated potential distribution diagram of the point-charge physical model. (C) A schematic diagram of electrons flow of IEB-TENG per cycle. (D) The short-circuit current of IEB-TENG per cycle. (E) Schematic diagram of potential measurement at the front and the back of the slider. <i></i> The method for measuring the potential distribution; <ii></i> the electric potential on the dielectric surface when the slider moves in different directions. (F) The relationship of output charge of IEB-TENG and sliding displacement. <i></i> The schematic diagram of the IEB-TENG moves at different sliding regions; <ii></i> the output charge of IEB-TENG at different sliding displacements. (G) Responded signals of IEB-TENG at different sliding regions, including the full region and half (left or right) region. <i></i> The schematic diagram of the full region and half region; <ii></i> the short-circuit current of IEB-TENG in different sliding regions.

when the slider moves left, electrode ② shows positive potential, and electrode ① shows negative potential. The result shows that the potential at the front and back ends of slider is indeed opposite and changing the moving direction of slider does change the potential distribution. Moreover, if triboelectric materials of the slider and stator are reversed, then the surface potential is also reversed (fig. S15 and note S10). Therefore, the charge polarity of two triboelectric

materials and the relative moving direction of slider corporately determine the distribution of net positive and negative charge domains and further control the direction of output current.

The relationship of output charge of IEB-TENG and sliding displacement also suggests the new working mechanism of IEB-TENG. The output charge increases with the sliding distance because of the larger friction area (Fig. 2F). In addition, if the slider periodically moves on

the two sides of the conductive wire, then the IEB-TENG produces four output current groups and two output charge groups (Fig. 2G, <ii>, and fig. S16), while there are only two output current groups and one output charge group when the slider periodically moves on one side (left or right) of the conductive wire (detailed information can be found in figs. S17 to S19 and notes S11 and S12). Specifically, the change of moving direction also causes the reversed output current, which further demonstrates the results in Fig. 2E. The IEB-TENG also exhibits an excellent durability, and its output charge keeps stable even after 38,000 working cycles (fig. S20).

### Regulating the output performance of IEB-TENG

To further demonstrate the working mechanism and improve performance of IEB-TENG, we systematically optimize its structural parameters (the sliding speed is  $0.06 \text{ m s}^{-1}$ ; fig. S21) (Fig. 3A), including the geometry of slider ( $G$ ), the area of slider ( $A$ ), the width of slider ( $W$ ), the length of slider ( $L$ ), the external force ( $F$ ), the diameter of conductive wire ( $D$ ), and the buried depth of conductive wire ( $H$ ; the vertical distance between the conductive wire and triboelectric interface). As shown in Fig. 3B and fig. S22, the short-circuit charge and open-circuit voltage of IEB-TENG decrease as  $H$  increases (fig. S23 and note S13), because of the decreased induced charges by larger induction distance [ $U_{\text{wire}} = \frac{q}{4\pi\epsilon_0} \left( \frac{1}{\sqrt{H^2}} - \frac{1}{\sqrt{H^2+l^2}} \right)$ ]; here,  $q$  is the quantity of point charge,  $\epsilon_0$  is the permittivity of vacuum, and  $l$  represents the distance between point charges], which consists with the theoretical analysis (fig. S24 and note S14).  $D$  (here,  $0.025 \text{ mm} < D < 6 \text{ mm}$ ) basically has no effect on the output performance of IEB-TENG since the conductive wire is an equipotential body (Fig. 3C, fig. S25, and note S15). Therefore,  $D$  can even be  $25 \mu\text{m}$  or smaller (thinner than a hair), showing the potential to realize an efficient IEB-TENG by simple integration.

According to theoretical analysis of the point-charge physical model, the voltage of IEB-TENG is related to the separation distance of positive and negative charge domains. When the charge quantity is constant, the higher voltage is achieved in the larger separation distance (Fig. 3D). Notably, the experimental result (Fig. 3E, <i>) also shows that the output voltage of IEB-TENG does increase with  $W$ , but it eventually tends to a stable value because of the unavoidable parasitic capacitance ( $C_p$ ) parallelly connected with the measuring device in actual test circuit. Here, the relationship of the ideal voltage of IEB-TENG ( $V_{\text{ideal}}$ ), the voltage of  $C_p$  ( $V_p$ ), and the measured voltage of IEB-TENG ( $V_{\text{TENG}}$ ) can be depicted in an electric circuit (Fig. 3F). As  $W$  increases,  $V_{\text{TENG}}$  first increases and then is limited at the maximum parasitic voltage ( $V_{p,\text{max}}$ ) (Fig. 3E, <ii>; fig. S26; and note S16). We also designed an experiment to reveal the effect of  $C_p$  on output voltage of IEB-TENG. Given that output charges of IEB-TENG are stored in the parallel connected  $C_p$  and TENG's intrinsic capacitor,  $V_{\text{TENG}}$  and  $V_p$  have a strong relationship with  $Q_{\text{SC}}$  of IEB-TENG. They increase with  $Q_{\text{SC}}$  and lastly stabilize at a fixed value (Fig. 3G, <i>, and fig. S27). At a smaller  $L$ ,  $Q_{\text{SC}}$  is relatively small, so  $V_{\text{TENG}}$  is limited by  $C_p$ ; while a larger  $V_{\text{TENG}}$  is permitted at a larger  $L$  because there are enough charges (large  $Q_{\text{SC}}$ ) stored in  $C_p$  to realize a higher  $V_p$ . Considering that  $C_p$  cannot be fully removed,  $V_{\text{TENG}}$  increases with  $L$  and then to a stable value, which is close to the  $V_{\text{ideal}}$  (Fig. 3G, <ii>; fig. S28; and note S17). These results not only indicate that  $V_{\text{TENG}}$  of IEB-TENG is easily affected by  $V_{p,\text{max}}$  but also support the new working mechanism about output voltage of IEB-TENG based on the point-charge physical model.

Moreover, as shown in Fig. 3H, the output charge and voltage of IEB-TENG increase with  $F$  because of the increased triboelectric charge density. On the basis of the point-charge physical model, the different  $G$  values with same slider area does not affect the output performance of IEB-TENG (Fig. 3I), exhibiting an excellent shape adaptability of IEB-TENG. The output charge and voltage of IEB-TENG increase simultaneously as the area of slider increases (Fig. 3J and fig. S29), resulting in an average power density of  $0.89 \text{ W m}^{-2} \text{ Hz}^{-1}$  at the area of  $24 \text{ cm}^2$  with PTFE and PA as triboelectric material pair. The enhanced average power density of IEB-TENG at a larger slider area is attributed to the nearly stable charge density and the greatly increased output voltage because average power density is proportional to charge density and voltage. It is noted that the power density of conventional TENGs keeps stable or decreases with the increase in slider area (36, 37), depending on the stable charge density or decreased charge density, respectively (fig. S30 and note S18). This demonstrates the superiority of IEB-TENG in the preparation of large size harvester.

The IEB-TENG also shows the characteristics of broad materials selection (Fig. 4). The quantified triboelectric series for IEB-TENG, containing 72 paired dielectric materials measured under a relatively constant environmental condition (external force, 20 N; temperature, 296 to 300 K; relative humidity, 15 to 30%) (note S19) (15, 38–41), is also established for guiding the design of high-performance TENGs with double dielectric materials as triboelectric layers (note S20 and table S1), in which both charge polarity and charge quantity are simultaneously considered. Combined with material optimization and large area design to improve output charge and voltage, the IEB-TENG with the materials of PTFE and PET in  $24 \text{ cm}^2$  achieves an excellent output performance of 480 nC, 1.5  $\mu\text{A}$ , and 10 kV (fig. S31), and an average power density as high as  $2.02 \text{ W m}^{-2} \text{ Hz}^{-1}$  is realized (Fig. 3K), showing great potential of IEB-TENG for high-voltage applications and powering electronics.

### A new signal processing strategy and high-voltage applications of IEB-TENG

On the basis of the excellent output performance and the characteristic of four current signals per cycle of IEB-TENG, a new signal processing strategy is proposed for signal rectification. The output signals are separated into two noninterfering portions by high-voltage diodes: the positive output portion and negative output portion (Fig. 5A), which is more efficient than conventional methods based on one rectifier bridge (fig. S32 and note S21), and so it can simultaneously charge two capacitors (44 nF) to 10 kV, respectively (Fig. 5B and fig. S33). It is clear that each capacitor is charged twice per cycle by the IEB-TENG. Specifically, in the half of one working cycle, the capacitor in the positive output portion of IEB-TENG is firstly charged, and then the capacitor in the negative output portion of IEB-TENG is charged (Fig. 5C). This result is exactly consistent with the potential regions where the conductive wire locates in motion process. In addition, there is a voltage platform between the two charging processes. The reason is that the capacitor is only charged in the high potential region ( $V_{\text{TENG}} > V_{\text{capacitor}}$ ), while it cannot be charged in the low potential region ( $V_{\text{TENG}} < V_{\text{capacitor}}$ ) (fig. S34). The proportion of the voltage platform also increases from 6.9 to 26.5% when the voltage of capacitor increases from 2 to 10 kV (Fig. 5, D and E). That is, the effective charging time is shortened as the voltage of capacitor increases, and the voltage of capacitor increases quickly and then slowly because of the gradual decrease in potential difference between the capacitor and IEB-TENG (note S22).

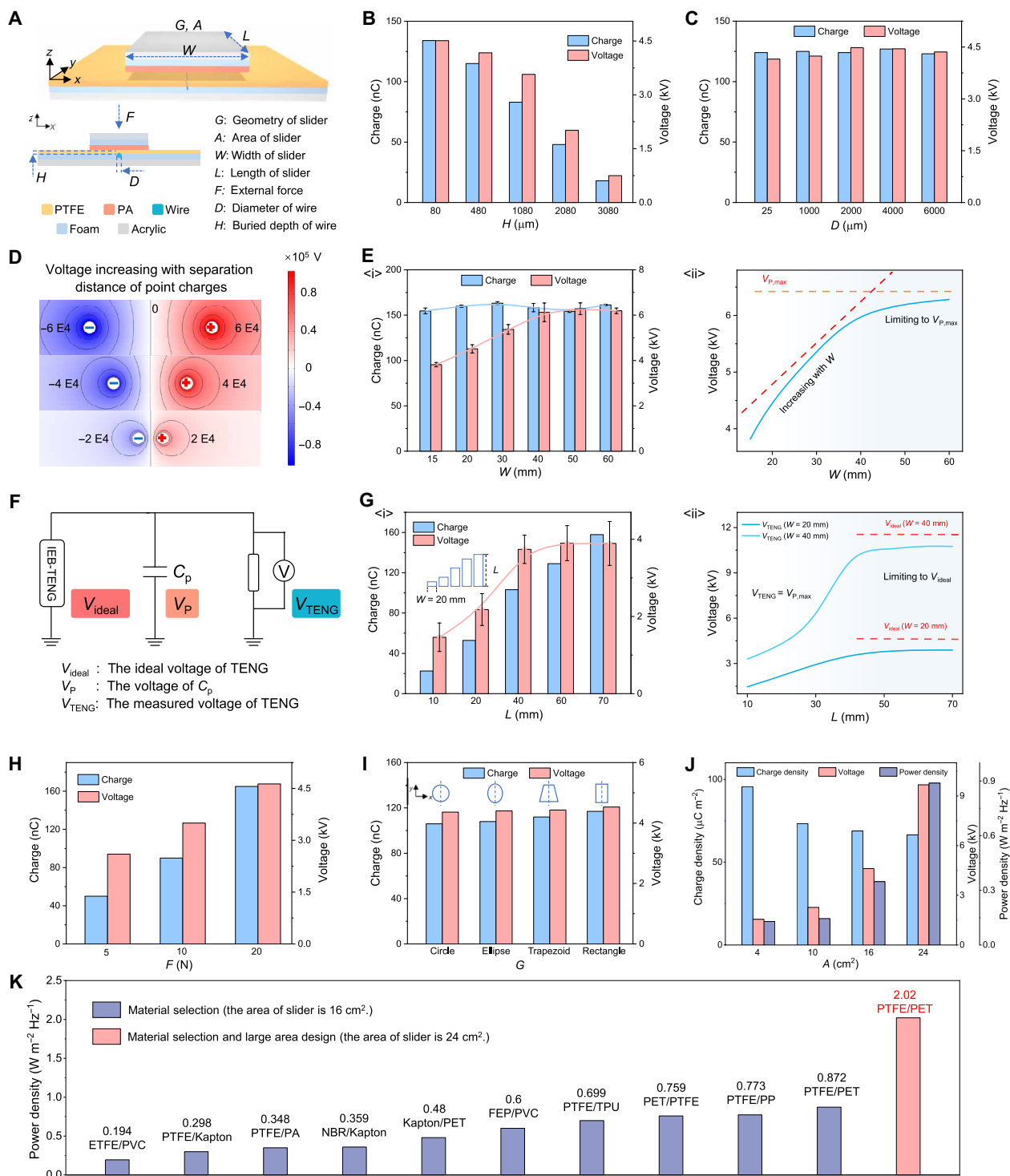


**Fig. 3. Regulating the output performance of IEB-TENG.** (A) Schematic diagram shows the various structure and motion parameters of IEB-TENG. (B) The short-circuit charge and open-circuit voltage of IEB-TENG with the conductive wire in different buried depths. (C) The short-circuit charge and open-circuit voltage of IEB-TENG with the conductive wire with different diameters. (D) Potential simulation diagram of point charge at different distances. (E) The effect of slider's width on the voltage of IEB-TENG. <i></i> The short-circuit charge and open-circuit voltage of IEB-TENG at different widths of slider ( $14 \text{ cm}^2$ ); <ii> the  $V_{\text{TENG}}$  of IEB-TENG at different widths of slider. The red dashed line is a schematic curve of  $V_{\text{ideal}}$ . (F) The relationship between the three voltages, including the  $V_{\text{ideal}}$ ,  $V_{P,\text{max}}$  and  $V_{\text{TENG}}$ . (G) The effect of slider's length on the voltage of IEB-TENG. <i></i> The short-circuit charge and open-circuit voltage of IEB-TENG at different lengths of slider (here,  $W = 2 \text{ cm}$ ); <ii> the  $V_{\text{TENG}}$  of IEB-TENG at different lengths of slider. The red dashed line is a schematic curve of  $V_{\text{ideal}}$ . (H) The short-circuit charge and open-circuit voltage of IEB-TENG at different external forces. (I) The short-circuit charge and open-circuit voltage of IEB-TENG with different geometries of the slider (here, the area of slider is  $14 \text{ cm}^2$ ). (J) The output charge density, open-circuit voltage, and average power density of IEB-TENG with different areas of slider. (K) The average power density of IEB-TENG with different dielectric material pairs.

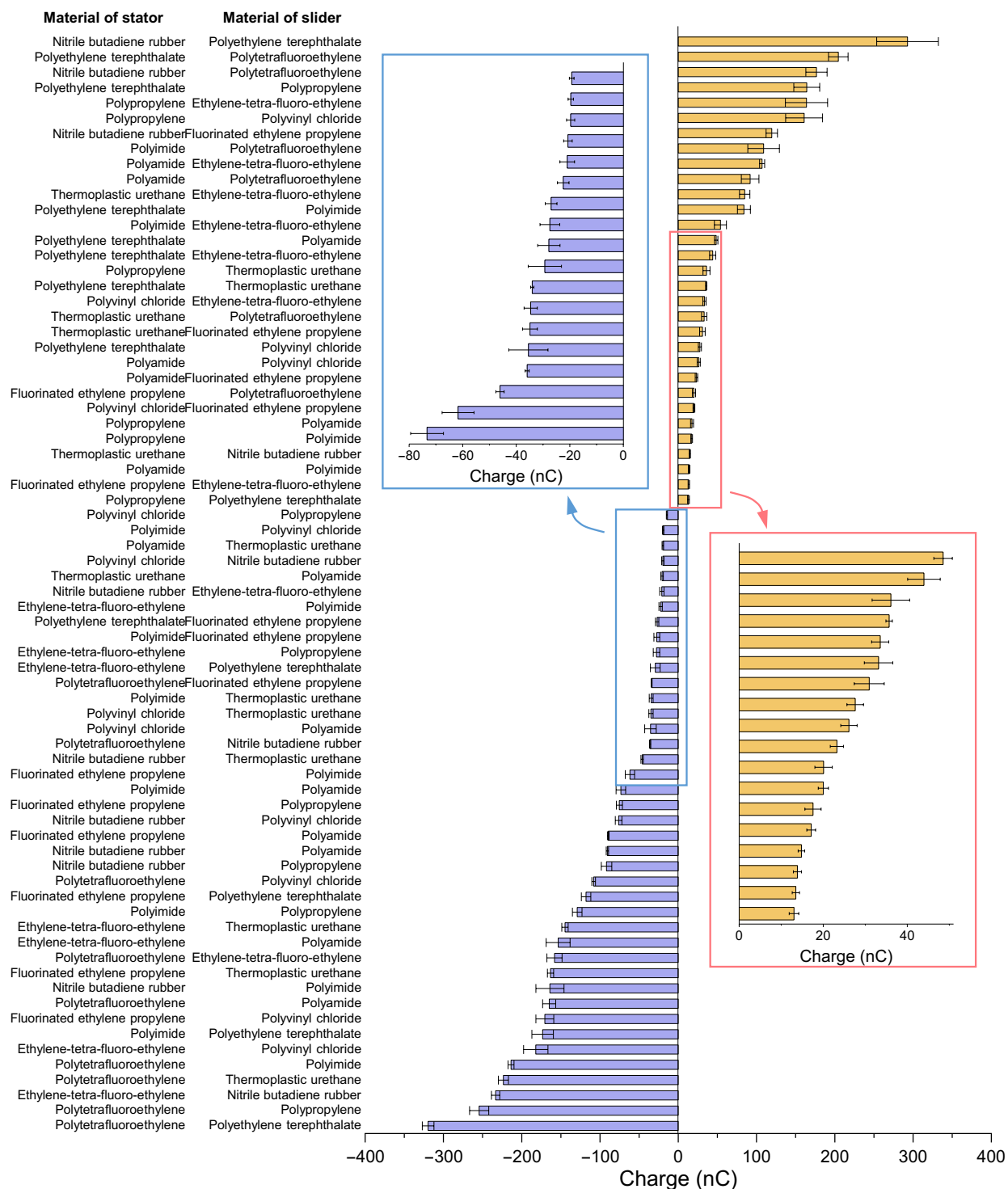
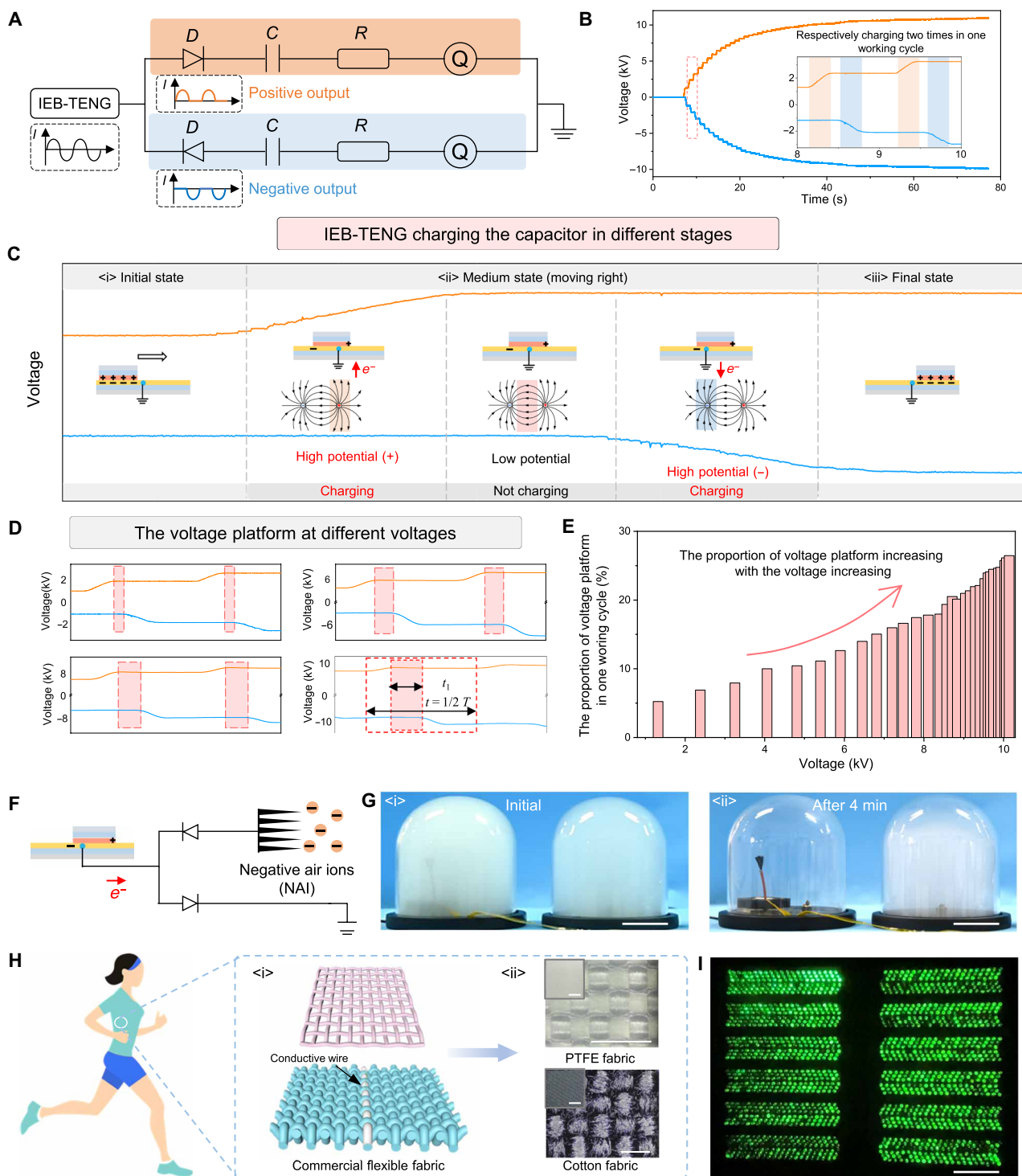


Fig. 4. Quantified triboelectric material pairs for the IEB-TENG. Error bars represent SD, n = 10 trials.

Beneficial from the high-voltage characteristic of IEB-TENG, it can be directly used as a new high-voltage power source with simple structure. As shown in fig. S35, IEB-TENG (the device area is 24 cm<sup>2</sup>) not only can simultaneously light two groups of 1512 LEDs after separated signal (movie S3) but also can directly light 3024 LEDs (fig. S36 and movie S4). Moreover, the high-voltage of IEB-TENG can

be used for efficient air pollution treatment (Fig. 5F). Compared with the control group, the IEB-TENG exhibits a better dust removal efficiency (Fig. 5G and movie S5), showing an application prospect in environmental economics. Beneficial from the simple structure and the adaptive conductive wire width, IEB-TENG can directly use commercial fabric as the triboelectric layer with the conductive wire



**Fig. 5. A new signal processing strategy and high-voltage applications of IEB-TENG.** (A) The circuit diagram of IEB-TENG with signal separation for charging electronics respectively. (B) The voltage of capacitor (44 pF) charged by IEB-TENG. Inset figure is one charging cycle by IEB-TENG. (C) The detailed charging process of capacitor during half of one working cycle of IEB-TENG. (D) The change of voltage platform with the different voltages of capacitor. (E) The proportion of voltage platform per cycle when the voltage of capacitor increases. (F) The circuit diagram of the IEB-TENG as a high-voltage power source to generate negative air ions. (G) The comparison of dust removal effect with and without IEB-TENG in initial state <i>i</i> and after 4 min <i>ii</i>. The mass of the smoke block is 0.1 g. Scale bars, 5 cm. (H) The IEB-TENG in wearable field. <i>i</i> Three-dimensional structure diagrams of textile fabrics; <i>ii</i> optical microscopic images of cotton fabric (material of stator) and PTFE fabric (material of slider) (scale bars, 1 mm). The scale bars in illustration are 1 cm. (I) The photo of 1512 LEDs lighted up by the IEB-TENG with commercial cotton fabric and PTFE fabric as triboelectric layers. Scale bar, 10 cm.

sewn into it (Fig. 5H, <i></i>), which can be used for timely harvesting human-movement mechanical energy for powering wearable electronics, simultaneously having properties such as air permeability, moisture resistance, and washable stability (fig. S37) (42, 43). As shown in Fig. 5H (<i></i>), using commercial cotton fabric and PTFE fabric as triboelectric layers (fig. S38), the wearable IEB-TENG shows output performance of 50 nC and 2.5 kV (fig. S39) and easily powers 1512 LEDs (Fig. 5I and movie S6). Furthermore, the conductive wire can be substituted with water-resistant and stretchable conductive fiber (44, 45), pointing a great application potential of IEB-TENG as self-powered system in intelligent wearable field.

### High-efficient PMC for IEB-TENG

The IEB-TENG not only can be directly used as a high-voltage power source but also can combine with the new signal processing method and a specially designed PMC to realize effective powering small electronics in internet of things. As shown in Fig. 6A, the energy generated by IEB-TENG is firstly stored in an input capacitor ( $C_{in}$ ) after the signal separated. Then, the energy conversion from  $C_{in}$  to the inductor ( $L$ ) is realized by a gas discharge tube (GDT). Last, the energy stored in  $L$  is transferred to the output capacitor ( $C_{out}$ ). A GDT of 5000 V is directly used rather than complex circuit elements to decrease energy loss (46, 47) because the IEB-TENG has a maximum average power at 5000 V (fig. S40), and it achieves four discharge times per cycle combined with the  $C_{in}$  (fig. S41). With  $C_{in}$  of 73.3 pF and  $C_{out}$  of 10  $\mu$ F, the IEB-TENG can produce the output voltage of 30 V and the stable output current as high as 29  $\mu$ A in the external load ( $R = 1$  megohm) (Fig. 6B). When the external load is 1 kilohm, a high peak current of 10 mA can also be obtained to meet requirements for high-power electronics (Fig. 6C). The average power of IEB-TENG with optimized PMC can reach to 1.6 mW (fig. S42), and the PMC achieves an energy conversion efficiency up to 87.3% (Fig. 6D and note S23). With the PMC, the capacitor of 10  $\mu$ F can be quickly charged to 39 V in 10 s with a 3563-fold greater stored energy of about 7.66 mJ (Fig. 6E and fig. S43). Furthermore, the IEB-TENG with PMC also displays an excellent performance in the required voltage range of common electronics (0 to 30 V) (Fig. 6F), and the output power has been greatly improved, such as 763-fold at 1.5 V (977 and 1.28  $\mu$ W), 116-fold at 12 V (1380 and 11.91  $\mu$ W), and 60-fold at 24 V (1536 and 25.64  $\mu$ W), which suggests that the IEB-TENG with the PMC is capable and suitable for powering variable electronics with different power requirements.

Beneficial from the high-energy conversion efficiency of the PMC, the IEB-TENG can be used as a micro/nano energy source to form a self-powered system. As shown in fig. S44, the system consists of an IEB-TENG (the energy source), two PMC ( $C_{out}$  of 2.2 mF), and 16 thermohygrometers (the energy consumption unit). With the fast charging speeds of 186.3 and 197.8  $\mu$ C s<sup>-1</sup>, the capacitors can be quickly charged to about 1.5 V after 17 s (Fig. 6H). The 16 thermohygrometers are respectively powered (Fig. 6G and movie S7) and can work stably for more than 15 min (fig. S45), which shows the potential of IEB-TENG for long-term and stable power supply for internet of things.

### DISCUSSION

In summary, a paradigm-shift energy harvesting strategy is proposed to efficiently harvest the electrostatic energy of dynamic IEB with a single conductive wire embedded into dielectric materials based on electrostatic induction. The observation method for characterizing

the IEB phenomenon is also presented, and the experimental results indicate that the distributed IEB can approach and gather to a conductive wire, realizing the regulation and control of disordered IEB. Moreover, we propose a point-charge physical model to explain the new principle of energy harvester and systematically verify it from theoretical analysis and experimental measurements, offering a paradigm-shift TENG: IEB-TENG. It is noted that the IEB-TENG unlocks the restriction of electrostatic breakdown on the performance of conventional TENGs, which produces electricity by directly using the IEB based on electrostatic induction. On the basis of systematic optimization of material, structure, and motion parameters, the designed IEB-TENG achieves a high voltage over 10 kV and an average power density as high as 2.02 W m<sup>-2</sup> Hz<sup>-1</sup>, which is 5.4 to 18.7 times higher than that of conventional TENGs. A quantified triboelectric series with 72 paired dielectric materials is also established for guiding practical applications. Furthermore, on the basis of the output characteristics of IEB-TENG and the new signal processing method, it not only can be used as high-voltage power sources for powering 3024 LED blubs and efficient dust removal but also can be combined with a specially designed PMC (energy conversion efficiency, 87.3%) to form a self-powered system for stably powering 16 thermohygrometers. IEB-TENG can be successfully integrated in wearable fabrics to harvest human mechanical energy as smart clothing. Briefly, this work not only opens a door for harvesting electrostatic energy arising from dynamic IEB but also offers valuable insights IEB, and even other any unexplored IEB, pioneering a potential path for innovative applications in high-voltage power sources, smart clothing, and internet of things.

### MATERIALS AND METHODS

#### Fabrication of the IEB-TENG

The IEB-TENG consists of a stator and a slider. For the stator, a rectangular acrylic sheet was cut as the substrate (90 mm by 60 mm; thickness, 5 mm) using a laser cutter (PLS6.75, Universal Laser System). A piece of foam (thickness, 3 mm) of the same size was adhered to the substrate to form a soft contact. A single conductive wire (diameter, 25  $\mu$ m; length, 70 mm) was placed right in the middle of the length of the stator. The triboelectric material was adhered on the surface of the foam as the triboelectric layer. For the slider, a rectangular acrylic sheet (thickness, 5 mm) was cut as the substrate (32 mm by 50 mm) using the laser cutter. The foam of the same size was adhered to the substrate to form a soft contact. The triboelectric material was adhered on the surface of the foam as the other triboelectric layer.

#### Fabrication of the IEB-TENG with different parameters

For the IEB-TENG with different triboelectric material pairs, we changed the triboelectric materials of stator and slider and used the same method to fabricate these TENGs. For the IEB-TENG with different  $H$  values, the depth was controlled by the fixed thickness of PTFE and foam. For the IEB-TENG with different diameters of conductive wire, cut the copper foil (thickness, 50  $\mu$ m; length, 7 mm) as conductor with the width of 1, 2, 4, and 6 mm. The 25- $\mu$ m conductive wire used in this work is commercial stainless steel wire. The different external forces were achieved by weights of different qualities. For the IEB-TENG with different shapes of slider, the radius of circle is 2.26 cm; the major and minor axes of the ellipse are 5.1 and 2 cm, respectively; the upper bottom, lower bottom, and height of the trapezoid are 3, 5, and 4 cm, respectively. For the IEB-TENG with

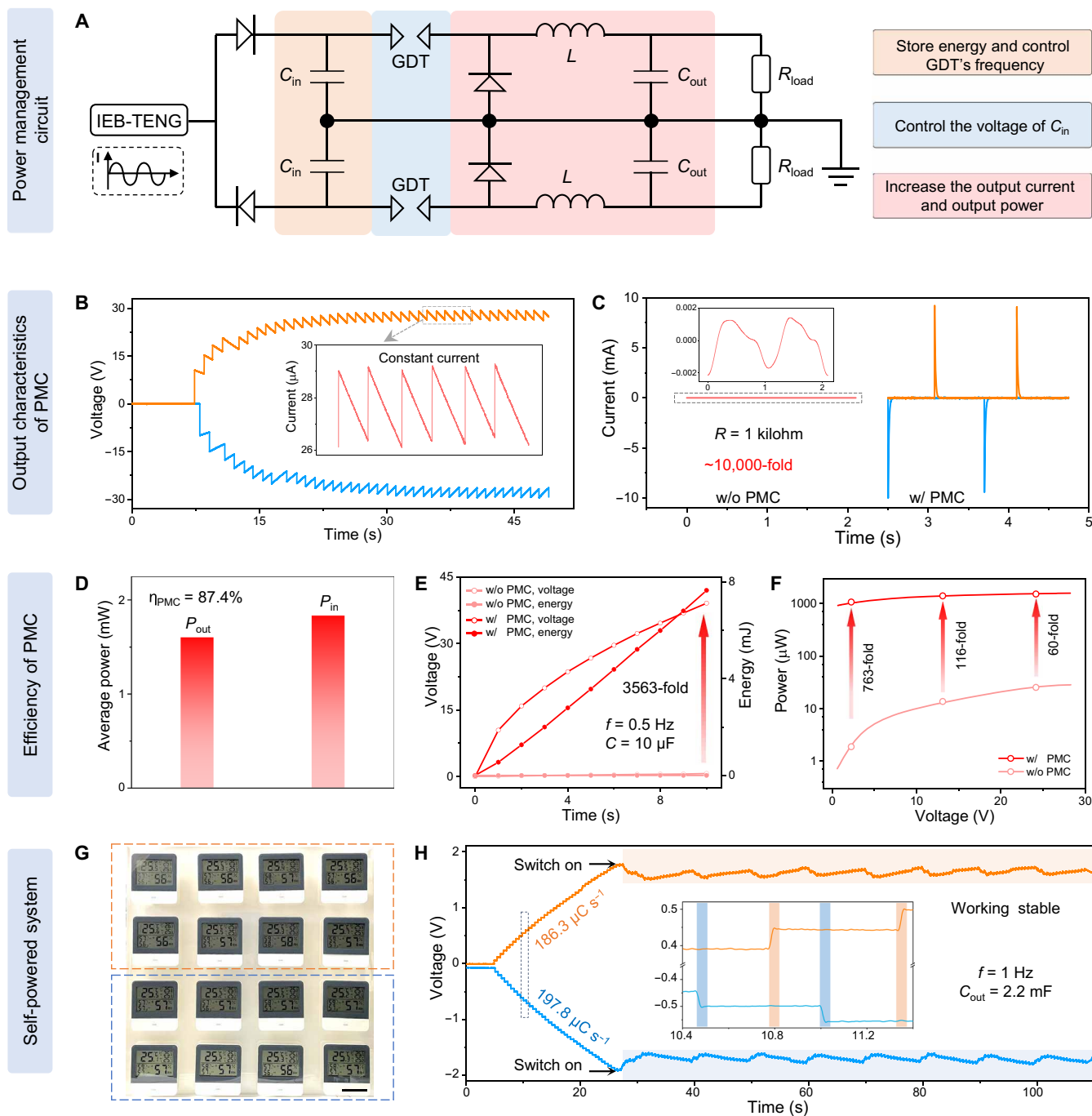


**Fig. 6. PMC for IEB-TENG and its application as a micro/nano energy source.** (A) PMC diagram for IEB-TENG. (B) The output voltage of IEB-TENG with the PMC ( $R = 1$  megohm). (C) The output current of IEB-TENG with (w/) and without (w/o) PMCs at the resistance of 1 kilohm. (D) The energy conversion efficiency of the PMC. (E) The voltage and energy of capacitor ( $10 \mu\text{F}$ ) charging by the IEB-TENG with and without the PMC in the positive output portion. (F) The output power of the IEB-TENG at required voltage range of common electronics (0 to 30 V) with and without the PMC. (G) Photograph of 16 commercial thermohygrometers powered by the IEB-TENG with the PMC. Scale bar, 5 cm. (H) The monitoring voltage curves of capacitors charging by IEB-TENG with the PMC (the working frequency is 1 Hz).

different areas of slider, the sliders are 20 mm by 20 mm ( $4 \text{ cm}^2$ ), 20 mm by 50 mm ( $10 \text{ cm}^2$ ), 32 mm by 50 mm ( $16 \text{ cm}^2$ ), and 40 mm by 60 mm ( $24 \text{ cm}^2$ ). For the IEB-TENG as wearable generator, the material of slider is commercial PTFE fabric. The material of stator is commercial black cotton cloth, and the conductive wire is sewn into cloth by a sewing machine.

### Simulation of electrostatic breakdown in microscale gap

To intuitively express that low charge density easily causes microscale breakdown, a plane-parallel capacitor model was built by the COMSOL software. According to the theory of air breakdown, Paschen's law, when the separation distance of two charged materials is  $15 \mu\text{m}$ , the breakdown can occur with a charge density only of

247  $\mu\text{C m}^{-2}$ . Similarly, when the separation distances are 25, 40, and 60  $\mu\text{m}$ , the charge density thresholds for electrostatic breakdown are 163, 125, 103  $\mu\text{C m}^{-2}$ , respectively.

### Simulation of the point-charge physical model

The point-charge physical model was built by the COMSOL software. The charge of each point charge is 2  $\mu\text{C}$ , and the diameter of point charge is 2 mm. The relative dielectric constant of air is 1. The separation distance of point charges is 12 mm in Fig. 2B, and the equipotential lines are also marked. The separation distance of point charges in Fig. 3D is 4, 12, and 20 mm, respectively.

### Surface potential detecting

To detect the electric potential of the materials surface during the slider moving process, two surface potential detectors (Trek 347) are installed at both ends of the slider. The potential at both ends of the slider is measured simultaneously by two channels, and the net charge domain at both ends of the slider is judged according to the potential detection results.

### IEB video shoot

To clearly exhibits the process of IEB in triboelectric materials, a nearly all-black environment was constructed. The discharge photos were captured using the long exposure method of a digital camera (Nikon D750), and the corresponding parameters is F4, ISO H2.0, and exposure with 10 s. The video of IEB between the materials was shoot with the parameters of F4 and ISO H2.0.

### Characterization

The sliding process was controlled by a liner motor (TSMV120-1S, LinMot). The amount of transferred charge and short-circuit current of TENGs were measured by a programmable electrometer (Keithley 6514), the open-circuit voltage is obtained by a resistance of 50 gigohms multiplied by its current. The surface potential was detected by an electrostatic voltmeter (Trek 347). Equivalent capacitances are measured by a precision LCR meter (TH2838A). Characterizations of surface fluctuation are realized by an optical microscopy (Nikon LV-FM), a scanning electron microscope (Hitachi SU8020) and a surface profiler (DektakXT). The  $C_{in}$  of 73.3 pF in Fig. 6B was made up of three capacitors of 220 pF in series, and the withstand voltage of  $C_{out}$  is 10,000 V. Photos in this paper were taken with a digital camera (Nikon D750). Finite element method simulation was implement based on the COMSOL software.

### Supplementary Materials

#### This PDF file includes:

Supplementary Text  
Notes S1 to S23  
Figs. S1 to S45  
Table S1  
Legends for movies S1 to S7  
References

#### Other Supplementary Material for this manuscript includes the following:

Movies S1 to S7

### REFERENCES AND NOTES

- H. T. Baytekin, A. Z. Patashinski, M. Branicki, B. Baytekin, S. Soh, B. A. Grzybowski, The mosaic of surface charge in contact electrification. *Science* **333**, 308–312 (2011).
- R. G. Horn, D. T. Smith, A. Grabbe, Contact electrification induced by monolayer modification of a surface and relation to acid–base interactions. *Nature* **366**, 442–443 (1993).
- R. G. Horn, D. T. Smith, Contact electrification and adhesion between dissimilar materials. *Science* **256**, 362–364 (1992).
- J. Chen, Y. Huang, N. Zhang, H. Zou, R. Liu, C. Tao, X. Fan, Z. L. Wang, Micro-cable structured textile for simultaneously harvesting solar and mechanical energy. *Nat. Energy* **1**, 16138 (2016).
- D. M. Pai, B. E. Springett, Physics of electrophotography. *Rev. Mod. Phys.* **65**, 163–211 (1993).
- B. A. Kwetkus, K. Sattler, H. C. Siegmann, Gas breakdown in contact electrification. *J. Phys. D* **25**, 139–146 (1992).
- H. Tao, J. Gibert, Measuring gas discharge in contact electrification. *Nat. Commun.* **14**, 8100 (2023).
- R. De, G. Ananthakrishna, Dynamics of the peel front and the nature of acoustic emission during peeling of an adhesive tape. *Phys. Rev. Lett.* **97**, 165503–165506 (2006).
- R. Budakian, K. Weninger, R. A. Hiller, S. J. Putterman, Picosecond discharges and stick–slip friction at a moving meniscus of mercury on glass. *Nature* **391**, 266–268 (1998).
- C. G. Camara, J. V. Escobar, J. R. Hird, S. J. Putterman, Correlation between nanosecond x-ray flashes and stick–slip friction in peeling tape. *Nature* **455**, 1089–1092 (2008).
- Z. L. Wang, A. C. Wang, On the origin of contact-electrification. *Mater. Today* **30**, 34–51 (2019).
- A. McAdie, Franklin's kite experiment and the energy of lightning. *Mon. Weather Rev.* **56**, 216–219 (1928).
- Z. L. Wang, On the expanded Maxwell's equations for moving charged media system—General theory, mathematical solutions and applications in TENG. *Mater. Today* **52**, 348–363 (2022).
- F.-R. Fan, Z.-Q. Tian, Z. Lin Wang, Flexible triboelectric generator. *Nano Energy* **1**, 328–334 (2012).
- D. Liu, L. Zhou, S. Cui, Y. Gao, S. Li, Z. Zhao, Z. Yi, H. Zou, Y. Fan, J. Wang, Z. L. Wang, Standardized measurement of dielectric materials' intrinsic triboelectric charge density through the suppression of air breakdown. *Nat. Commun.* **13**, 6019 (2022).
- H. Li, A. Berbille, X. Zhao, Z. Wang, W. Tang, Z. L. Wang, A contact-electro-catalytic cathode recycling method for spent lithium-ion batteries. *Nat. Energy* **8**, 1137–1144 (2023).
- Y. Yang, X. Guo, M. Zhu, Z. Sun, Z. Zhang, T. He, C. Lee, Triboelectric nanogenerator enabled wearable sensors and electronics for sustainable internet of things integrated green earth. *Adv. Energy Mater.* **13**, 2203040 (2023).
- T. He, H. Wang, J. Wang, X. Tian, F. Wen, Q. Shi, J. S. Ho, C. Lee, Self-sustainable wearable textile nano-energy nano-system (NENS) for next-generation healthcare applications. *Adv. Sci.* **6**, 1901437 (2019).
- D. Liu, X. Yin, H. Guo, L. Zhou, X. Li, C. Zhang, J. Wang, Z. L. Wang, A constant current triboelectric nanogenerator arising from electrostatic breakdown. *Sci. Adv.* **5**, eaav6437 (2019).
- C. Shan, W. He, H. Wu, S. Fu, Q. Tang, Z. Wang, Y. Du, J. Wang, H. Guo, C. Hu, A high-performance bidirectional direct current TENG by triboelectrification of two dielectrics and local corona discharge. *Adv. Energy Mater.* **12**, 2200963 (2022).
- A. Chen, Q. Zeng, L. Tan, F. Xu, T. Wang, X. Zhang, Y. Luo, X. Wang, A novel hybrid triboelectric nanogenerator based on the mutual boosting effect of electrostatic induction and electrostatic breakdown. *Energy Environ. Sci.* **16**, 3486–3496 (2023).
- L. Zhou, D. Liu, Z. Zhao, S. Li, Y. Liu, L. Liu, Y. Gao, Z. L. Wang, J. Wang, Simultaneously enhancing power density and durability of sliding-mode triboelectric nanogenerator via interface liquid lubrication. *Adv. Energy Mater.* **10**, 2002920 (2020).
- S. Cui, L. Zhou, D. Liu, S. Li, L. Liu, S. Chen, Z. Zhao, W. Yuan, Z. L. Wang, J. Wang, Improving performance of triboelectric nanogenerators by dielectric enhancement effect. *Matter* **5**, 180–193 (2022).
- J. Zhang, Y. Gao, D. Liu, J.-S. Zhao, J. Wang, Discharge domains regulation and dynamic processes of direct-current triboelectric nanogenerator. *Nat. Commun.* **14**, 3218 (2023).
- K. Dai, D. Liu, Y. Yin, X. Wang, J. Wang, Z. You, H. Zhang, Z. L. Wang, Transient physical modeling and comprehensive optimal design of air-breakdown direct-current triboelectric nanogenerators. *Nano Energy* **92**, 106742 (2022).
- Z. Zhao, L. Zhou, S. Li, D. Liu, Y. Li, Y. Gao, Y. Liu, Y. Dai, J. Wang, Z. L. Wang, Selection rules of triboelectric materials for direct-current triboelectric nanogenerator. *Nat. Commun.* **12**, 4686 (2021).
- R. Cheng, K. Dong, P. Chen, C. Ning, X. Peng, Y. Zhang, D. Liu, Z. L. Wang, High output direct-current power fabrics based on the air breakdown effect. *Energy Environ. Sci.* **14**, 2460–2471 (2021).
- Z. Zhao, Y. Dai, D. Liu, L. Zhou, S. Li, Z. L. Wang, J. Wang, Rationally patterned electrode of direct-current triboelectric nanogenerators for ultrahigh effective surface charge density. *Nat. Commun.* **11**, 6186 (2020).
- K. Li, C. Shan, S. Fu, H. Wu, W. He, J. Wang, G. Li, Q. Mu, S. Du, Q. Zhao, C. Hu, H. Guo, High efficiency triboelectric charge capture for high output direct current electricity. *Energy Environ. Sci.* **17**, 580–590 (2024).

30. Q. Zeng, A. Chen, X. Zhang, Y. Luo, L. Tan, X. Wang, A dual-functional triboelectric nanogenerator based on the comprehensive integration and synergetic utilization of triboelectrification, electrostatic induction, and electrostatic discharge to achieve alternating current/direct current convertible outputs. *Adv. Mater.* **35**, e2208139 (2023).
31. Y. Gao, D. Liu, Y. Li, J. Liu, L. Zhou, X. Li, Z. Zhao, S. Li, P. Yang, Z. L. Wang, J. Wang, Achieving high-efficiency triboelectric nanogenerators by suppressing the electrostatic breakdown effect. *Energy Environ. Sci.* **16**, 2304–2315 (2023).
32. D. Liu, L. Zhou, Z. L. Wang, J. Wang, Triboelectric nanogenerator: From alternating current to direct current. *iScience* **24**, 102018 (2021).
33. Y. I. Sobolev, W. Adamkiewicz, M. Siek, B. A. Grzybowski, Charge mosaics on contact-electrified dielectrics result from polarity-inverting discharges. *Nat. Phys.* **18**, 1347–1355 (2022).
34. H. Qin, L. Xu, F. Zhan, Z. L. Wang, Electron transfer induced contact-electrification at oil and oleophobic dielectric interface. *Nano Energy* **116**, 108762 (2023).
35. H. Qin, L. Xu, S. Lin, F. Zhan, K. Dong, K. Han, H. Wang, Y. Feng, Z. L. Wang, Underwater energy harvesting and sensing by sweeping out the charges in an electric double layer using an oil droplet. *Adv. Funct. Mater.* **32**, 2111662 (2022).
36. Y. Zi, S. Niu, J. Wang, Z. Wen, W. Tang, Z. L. Wang, Standards and figure-of-merits for quantifying the performance of triboelectric nanogenerators. *Nat. Commun.* **6**, 8376 (2015).
37. S. Niu, S. Wang, L. Lin, Y. Liu, Y. S. Zhou, Y. Hu, Z. L. Wang, Theoretical study of contact-mode triboelectric nanogenerators as an effective power source. *Energy Environ. Sci.* **6**, 3576–3583 (2013).
38. L. Liu, L. Zhou, C. Zhang, Z. Zhao, S. Li, X. Li, X. Yin, J. Wang, Z. L. Wang, A high humidity-resistive triboelectric nanogenerator via coupling of dielectric material selection and surface-charge engineering. *J. Mater. Chem. A* **9**, 21357–21365 (2021).
39. L. Liu, Z. Zhao, Y. Li, X. Li, D. Liu, S. Li, Y. Gao, L. Zhou, J. Wang, Z. L. Wang, Achieving ultrahigh effective surface charge density of direct-current triboelectric nanogenerator in high humidity. *Small* **18**, e2201402 (2022).
40. D. Liu, L. Zhou, S. Li, Z. Zhao, X. Yin, Z. Yi, C. Zhang, X. Li, J. Wang, Z. L. Wang, Hugely enhanced output power of direct-current triboelectric nanogenerators by using electrostatic breakdown effect. *Adv. Mater. Tech.* **5**, 2000289 (2020).
41. S. Lin, L. Xu, C. Xu, X. Chen, A. C. Wang, B. Zhang, P. Lin, Y. Yang, H. Zhao, Z. L. Wang, Electron transfer in nanoscale contact electrification: Effect of temperature in the metal-dielectric case. *Adv. Mater.* **31**, e1808197 (2019).
42. M. E. Stoffberg, L. Hunter, A. Botha, The effect of fabric structural parameters and fiber type on the comfort-related properties of commercial apparel fabrics. *J. Nat. Fibers* **12**, 505–517 (2015).
43. S. V. Cheng, W. X. Hao, Y. C. Wang, Y. Wang, S. Yang, Commercial janus fabrics as reusable facemask materials: A balance of water repellency, filtration efficiency, breathability, and reusability. *ACS Appl. Mater. Interfaces* **14**, 32579–32589 (2022).
44. Z. Wang, Z. Wang, D. Li, C. Yang, Q. Zhang, M. Chen, H. Gao, L. Wei, High-quality semiconductor fibres via mechanical design. *Nature* **626**, 72–78 (2024).
45. M. Chen, Z. Wang, Q. Zhang, Z. Wang, W. Liu, M. Chen, L. Wei, Self-powered multifunctional sensing based on super-elastic fibers by soluble-core thermal drawing. *Nat. Commun.* **12**, 1416 (2021).
46. W. Harmon, D. Bamgboje, H. Guo, T. Hu, Z. L. Wang, Self-driven power management system for triboelectric nanogenerators. *Nano Energy* **71**, 104642 (2020).
47. H. Zhang, F. Marty, X. Xia, Y. Zi, T. Bourouina, D. Galayko, P. Basset, Employing a MEMS plasma switch for conditioning high-voltage kinetic energy harvesters. *Nat. Commun.* **11**, 3221 (2020).
48. S. Fu, C. Hu, Achieving ultra-durability and high output performance of triboelectric nanogenerators. *Adv. Funct. Mater.* **22**, 2308138 (2023).

#### Acknowledgments

**Funding:** This work was supported by the National Key R&D Project from Minister of Science and Technology (2021YFA1201602), National Natural Science Foundation of China (grant nos. 62204017 and U21A20147), China Postdoctoral Science Foundation (2021 M703172 and 2021 M703171), Innovation Project of Ocean Science and Technology (22-3-3-hygg-18-hy), and the Fundamental Research Funds for the Central Universities (E1E46802 and E1E46803). **Author contributions:** L.H., Y.G., D.L., and J.W. conceived the idea. L.H. and Y.G. performed the experiments and analyzed the data. Y.H., J.S., J.Z., X.L., and B.J. provided suggestions in preparing the pictures. L.H. and D.L. drafted the manuscript. J.W. revised the manuscript. D.L., J.W., and Z.L.W. supervised this work. All the authors discussed the results and commented on the manuscript. **Competing interests:** The authors declare that they have no competing interests. **Data and materials availability:** All data needed to evaluate the conclusions in the paper are present in the paper and/or the Supplementary Materials.

Submitted 9 February 2024

Accepted 8 May 2024

Published 12 June 2024

10.1126/sciadv.ado5362